Remnants and rates of metamorphic decarbonation in continental arcs

Evan J. Ramos, Jade Star Lackey, Jaime D. Barnes, and Anne A. Fulton

Support Information: GSA Data Repository 2020150

1) Volume estimates for sedimentary rocks, magmatic intrusions, metamorphic roof pendants, skarns, and metamorphic aureoles

a. Sedimentary rocks

i. *Sierra Nevada batholith (SNB)*

For the Sierra Nevada batholith, we compile stratigraphic thicknesses, rock types, and proportions from remnant stratigraphy preserved as metamorphosed wallrock pendants and septa in the Sierra Nevada. These include representative columns from the Triassic-Jurassic Kings Sequence (Saleeby and Busby, 1993) which is typical of rocks in the western Sierra; composite columns continental-margin metasedimentary rocks of the Morrison block (Stevens and Greene, 1999) in the eastern Sierra typify the Paleozoic stratigraphy into which parts of the eastern Sierran arc was built. To compute a volume of rock, we assume the rocks were present along the length and width of the area into which the active Cretaceous arc was constructed. This areal distribution, which are approximated from Lee et al. (2013) and Cao et al. (2017). The stratigraphic thickness multiplied by the area of the active Cretaceous arc yields a volume of sedimentary rocks.

ii. *North America*

We amass sedimentary rock types, proportions, ages, and volumes in North America through the Macrostrat geologic database (Peters et al., 2018). We access all sedimentary rock information from Macrostrat using this API command: https://macrostrat.org/api/v2/units?age_top=0&age_bottom=600&response=long. We classify all rock units as siliciclastic, carbonate, mixed carbonate-siliciclastic, and “other”, which itself is comprised of evaporites, batholiths, chemical, organic, and volcanic units. We exclude the volume of metamorphic rocks in our estimate of net stratigraphic volumes. Once each rock type is binned, we multiply their reported areal exposure [km^2] by their average stratigraphic thickness [km] to yield the sedimentary rock volume for each rock unit. All sedimentary rock volumes are corrected for erosion through a compensation model (*sensu* Cao et al., 2017) that uses an erosional half-life of 400 Myr, since the total volume of sedimentary rocks is thought to decay exponentially with time (Mackenzie and Garrels, 1971).

Given the roughly equivalent proportion of rock volumes across tectonic environments on continents, albeit slight differences in sedimentary proportions between Laurentian and Gondwanan crust (e.g. Ronov, 1982), we assume rock

types and distributions for North America are representative of global sedimentary rocks. Furthermore, the area of North America (25×10^6 km^2) is comparable to the area of all continental arcs present and past ($5 – 22 \times 10^6$ km^2, assuming range of arc lengths from Cao et al., 2017 and range of arc widths from Ducea et al., 2015), which enables a direct comparison of sedimentary rock volume to arc magma volume.

b. **Magmatic intrusions**

i. *Sierra Nevada batholith (SNB)*

1. Age refinement

This calculation of longitudinal arc magma productivity for the Cretaceous Sierra Nevada batholith is the first to calculate a Sierran magma flux with pluton-level area integration for both the central and southern Sierra Nevada batholith.

Estimates of magmatic flux are derived from age-based areas [km^2] of plutons in a corridor that spans shallow to lower crustal exposures from the central to southern Sierra Nevada batholith, respectively. This corridor runs from approximately Yosemite Valley to the Tehachapi Mountains (Fig. DR1). With inclusion of the southern Sierra Nevada and pluton-scale area integration, this measurement provides the most accurate and precise calculated magma flux of the Sierra to date, expanding threefold the areas used by Ratschbacher et al. (2019). The selection of this corridor was deemed the most reliable way to obtain estimates of magmatic flux because it met three important conditions: 1) availability of detailed maps pluton and wallrock extent; 2) a range of erosional levels that allow a general approximation of pluton:wallrock ratios from upper to lower crustal levels (Ague and Brimhall 1988; Nadin and Saleeby, 2008); and 3) sufficient geochronologic age coverage to designate reliable ages for most of the plutons in the region. Areas in the northern Sierra Nevada fail to meet these criteria because of cover of eroded batholithic rock by younger volcanic rocks or that erosion levels do not penetrate batholith rocks to reveal plutonic architecture. The wealth of geologic maps in the central and southern Sierra by USGS workers (Bateman, 1992; Moore and Sisson, 1987; Ross, 1987; 1989) allows for a precise calculation of area addition rates of plutons. Because many of the plutons in the central Sierra Nevada tend to be dike-like in morphology and relatively small, published U-Pb zircon ages can be assigned in general without major concerns about incremental emplacement patterns skewing age-designations of plutons.

The map included is largely based on a pluton map drafted by Lackey et al. (2008) that is based on 1x2° geologic map sheets of the Mariposa quadrangle (Bateman et al. 1992) and the simplified pluton map of most of the Fresno 1x2° sheet (Moore and Sisson,1987). Our new version incorporates mapped pluton areas in the southern Sierra Nevada that draw from work by Ross (1987;1989) whose work is much of the basis for the plutonic units that were extensively dated by U-Pb of zircon in Saleeby et al. (2008). Additional refinements in the west-central Sierra are from Sisson and Moore (2013).

Where modern single crystal or crystal population U-Pb zircon ages are available, these are adopted in lieu of prior regional U-Pb geochronology studies by Stern et al. (1981) and Chen and Moore (1982). For example, recent U-Pb ages in the southern Sierra (Saleeby et al., 2008) temporally contextualize Ross's (1987; 1989) plutonic mapping. In the northern area of the corridor, ages from Lackey et al. (2012) are used to define increments of the Fine Gold intrusive suite emplaced between 124 and 105 Ma. Ardill et al. (2018) summarize and add to the newer U-Pb age information for the Tuolumne Intrusive suite and rocks to the south. Ages for the large Mt. Givens granodiorite (Frazer et al. 2014) are used to subdivide it into areas of different age. Additional ages in the western and central Sierra (Lackey, unpublished) are included in detailed studies of tonalitic suites west of Sequoia National Park and in King Canyon.

2. Pluton area addition rates

Pluton area calculations are extracted by color-coding plutons or pluton domains for age in a vector graphics version of the map (Fig. DR1). This map was exported as a raster version with scaled features and analyzed in Adobe Photoshop®. The color ranges were selected for each age bin by tight ("fuzziness = 1") thresholding for pixel counts corresponding to pluton color. Individual pluton areas corresponding to plutons between 125 and 85 million years were integrated at 1 million-year intervals throughout the map corridor. This method effectively excludes undated, older, or younger plutons or roof pendants. Because of uncertainties of U-Pb ages that typically are 1%, it was found that areas computed for 1 million year "bins" tended to be irregular and noisy and that a running average of 3 million years provided the most realistic estimate of areal magma flux. For simple comparison to roof pendant area distributions, we present magma area vs. time. However, a volumetric magma flux could be computed by assuming a 50 km depth arc, which is a compromise between a nascent, thinner arc, and mature arc with a thick eclogite root (e.g., Ducea, 2001). To convert the areas to volumes that would decarbonate host rocks, we assume an average pluton thickness of 7km and multiply this value by the areas.

ii. *North America and Global*

We interpolate the granitoid area addition rates [km^2/Myr] from Cao et al., 2017 through time to get a time-continuous curve. We assume that all granitoid was emplaced evenly in the 3 to 13 km depth interval of the crust, or an emplacement thickness of 10 km. The stratigraphic thickness of sedimentary rocks in SNB is 7 km, so we instead assume all granitoid is emplaced evenly throughout the 7 km section. The area addition rate

multiplied by the emplacement thickness yields a volumetric addition rate of granitoid. All granitoid volumes are corrected for erosion through the same compensation model as was used for sedimentary rocks, using a 400 Myr half-life.

c. **Metamorphic roof pendants**

Whereas granitoid plutons form most of the Sierra Nevada batholith, fragments of metamorphic and volcanic rocks are often found as screens or steeply dipping septa between plutons (Saleeby et al. 1978; Moore and Sisson, 1987; Tobisch et al. 2000; Clemens-Knott et al. 2013). Many of these rocks in the west-central and southern Sierra are of the broadly defined “Kings Sequence” (Saleeby et al., 1978) which are assessed for typical carbonate contents in this study (Fig. DR2). These screens and pendants are commonly bounded by plutons of various ages, demonstrating that metamorphic wallrock is polymetamorphosed. These observations suggest that pendants have experienced multiple instances of decarbonation as plutons are constructed around them.

The absolute area of these pendants and screens is a fugitive quantity, however, based on the qualitative observation that the age of screens and pendants decrease in abundance within the younger portions of the batholith. To provide an estimate of the changing wallrock that plutons would encounter as the batholith was built, we measure wallrock availability in the form of a “pendant area isolation age”. This metric uses the age of youngest pluton that directly bounds a screen or pendant to assign an “isolation” age to that screen area. Two exceptionally large pendants that are excluded from our calculations are those of the Mount Goddard roof pendant, which is dominantly Jurassic rocks and surrounded by Jurassic plutons, and the Minarets volcanic sequence, which is mostly volcanic rock and relatively shallow, thereby acting more as a cover of the underlying batholith in this particular area. Our measured pendant area isolation ages show in general that the available wallrock into which the arc was constructed decreases with time. In addition, qualitatively, the proportion of metavolcanics pendant material tends to increase with decreasing age. Pendant isolation areas were calculated as a 3 million year running average with the same protocols employed for calculating the area of these pendants. Because the absolute area of exposed wallrocks is a minimum and excludes the shallow portions of the batholith, we adopt a normalized depiction of changing pendant area in the Cretaceous.

As is the case with the SNB magmas, we assume that the depths of the pendants are 7 km and thus the area of the plutons multiplied by this depth yields the pendant volumes. Some pendants in the SNB are greater than 7 km thick and can be found down to the base of the crust. Therefore, our minimum of 7 km, as determined by the summed stratigraphic thicknesses of the Kings Sequence and the Morrison block, is a conservative minimum thickness of roof pendants

d. Skarns and carbonates

We calculated skarn and carbonate relative volumes by digitizing geologic and tungsten deposit maps and cross sections from throughout the SNB. World War II strategic minerals investigation reports (e.g., Lemmon 1940, 1941) and other studies (Jenkins, 1943; Krauskopf, 1953) show detailed surface and sub-surface mapping and were useful estimations of carbonates as well as reacted carbonates. Proportions of skarn and marble were quantified from the digitized maps using ImageJ software thresholding for color-coded maps like the approach described above to obtain pluton areas.

e. Metamorphic aureoles

Our numerical model for oxygen isotope transport predicts the volume fraction of metamorphic aureole as a function of the volume fraction of granitoid (Fig DR3). Mathematically, the percentage of a host rock parcel γ that undergoes decarbonation is expressed as

$$\gamma(\delta^{18}\mathrm{O}) = \frac{\exp\left(\frac{1}{X_{\mathrm{CO_2}}} \cdot \frac{\delta^{18}\mathrm{O}_{max} - \delta^{18}\mathrm{O}}{\delta^{18}\mathrm{O}_{max} - \delta^{18}\mathrm{O}_{min}}\right)}{\exp\left(\frac{1}{X_{\mathrm{CO_2}}}\right) - 1} \quad (1)$$

where $X_{\mathrm{CO_2}}$ is the mole fraction of CO_2 in the aqueous phase (assumed to be equal to 0.15), $\delta^{18}\mathrm{O}_{max}$ is the $\delta^{18}O$ value of unaltered limestone (assumed to be equal to 22.75‰ VSMOW), $\delta^{18}\mathrm{O}_{min}$ is the $\delta^{18}O$ value of the igneous rocks (assumed to be equal to 5‰) and $\delta^{18}O$ is the $\delta^{18}O$ value of the host rock after hydrothermal activity has ceased. This value is spatially heterogeneous because the $\delta^{18}O$ value of the host rocks differ spatially (Fig. DR3B). The sum of γ, normalized to total volume of the domain (intrusion + host rock), yields the volume fraction of sedimentary rocks in the aureole $f_{aureole}$ that is decarbonated.

Considerable error in our prediction is introduced when crustal permeability changes over two orders of magnitude, yielding three disparate curves (Fig. 2 main text). For simplicity, when we apply these model predictions, we take the mean of the three curves and interpolate the curve to compute the volume fraction of the host rock that undergoes decarbonation.

2) Volume comparison for flux estimates

We compare a granitoid volume with a volume of sediments that likely encompass a depth interval. For the SNB flux estimates, we assume a depth interval of 7 km, corresponding to the stratigraphic thickness of the SNB sections (Fig. DR2). Our flux is computed by comparing the entire volume of sediment in that 7 km depth interval

and the cumulative volume of granitoid emplaced in that same depth interval over a 40 Myr time window from 125 – 85 Ma.

For our global flux estimates, we conservatively assume a 3–13 km depth interval over which most metamorphic decarbonation occurs. To determine which sediments are in that depth interval, we first assume that all sediments are buried at a continuous rate within the range of burial rates reported by Schumer and Jerolmack (2009). We then multiply the average depositional age of each rock unit reported in Macrostrat by the average burial rate to compute a depth for each rock unit. To get a volume of granitoid, we multiply the granitoid volume addition rate by the time interval over which we are comparing volumes.

We compare the volumes of the sedimentary rocks with the granitoids to determine the fraction of those rocks that are assimilated, $f_{assimilation}$ [L^3 L^{-3}], and decarbonated in the aureole, $f_{aureole}$ [L^3 L^{-3}]. Our foremost assumptions are that 1) all the sediments predate the emplacement of the intrusion and 2) they have not undergone metamorphism prior to the emplacement of the intrusion. Therefore, the volume of the sedimentary rock V_{sed} [L^3] is assumed to be the total volume of rocks in the shallow arc and upon emplacement of the intrusion,

$$V_{sed} = V_{host\ rock} + V_{intrusion} \tag{2}$$

where $V_{intrusion}$ [L^3] is the volume of the intrusion and $V_{host\ rock}$ [L^3] is the volume of the host rock remaining around the intrusion that can undergo contact metamorphism. We simply express $f_{assimilation}$ as

$$f_{assimilation} = \frac{V_{intrusion}}{V_{sed}} = \frac{V_{intrusion}}{V_{host\ rock} + V_{intrusion}} \tag{3}$$

which assumes that the entire volume of the intrusion assimilates an equivalent volume of the sedimentary rock in which it is emplaced. In all volume comparisons, V_{sed} is larger than $V_{intrusion}$. We express $f_{aureole}$ as

$$f_{aureole} = \frac{V_{aureole}}{V_{sed}} = \frac{V_{aureole}}{V_{host\ rock} + V_{intrusion}} \tag{4}$$

where $V_{aureole}$ is a function $V_{intrusion}$, as determined by our analogue decarbonation model (SI section 1e; Eq. 1).

3) Computing metamorphic decarbonation fluxes from continental arcs

We describe the net metamorphic decarbonation flux, F_{CO_2}[M T^{-1}], as the sum of the assimilation flux, $F_{assimilation}$, and the aureole decarbonation flux, $F_{aureole}$, where each flux can be expressed as

$$F_i = \frac{(1-\phi)\rho_{sed} V_{decarb,i}}{\Delta t} \quad (5)$$

where

$$V_{decarb,i} = f_i V_{sed} \sum_j \nu_j X_j, \quad (6)$$

ϕ [L^3 L^{-3}] is the average porosity of the sedimentary rocks, ρ_{sed} [M L^{-3}] is the average density of the sedimentary rocks, $V_{decarb,i}$ [L^3] is the volume of sedimentary rock that contributes to metamorphic flux i, f_i [L^3 L^{-3}] is the volume fraction of total sedimentary rock volume V_{sed} that is decarbonated, ν_j is the stoichiometric fraction of rock type j that can be converted to CO_2 [M M^{-1}], X_j is the volume fraction of rock type j comprising $V_{sed,i}$ [L^3 L^{-3}], and Δt is time interval over which the flux is approximated [T]. We integrate granitoid area addition rates over time, assuming a constant granitoid thickness and depth, to compute granitoid volumes. Lastly, through a Monte Carlo simulation, we consider the range of values for each above parameter to compute a statistically robust range of decarbonation fluxes through time (see Tables DR1-3 for parameter values). With no effective way to gauge how much metamorphic CO_2 exits the crust in the model, all computed metamorphic CO_2 fluxes represent maxima.

Table DR1. Parameter ranges and values used in metamorphic flux computations for both SNB and Phanerozoic flux estimates

Parameter [units]	**Value(s)**	**Reference**
Stoichiometric fraction for decarbonation of carbonate [mol/mol]	[0, 0.9]	Lee et al., 2013
Stoichiometric fraction for decarbonation of siliciclastic [mol/mol]	[0, 0.2]	--
Stoichiometric fraction for decarbonation of mixed [mol/mol]	[0, 0.7]	--
Stoichiometric fraction for assimilated flux [mol/mol]	[.08, .5]	Carter and Dasgupta, 2016
Porosity [km^3/km^3]	0.01	Allen and Allen, 2013
Sedimentary rock density [Mt/km^3]	2700	--

Table DR2. SNB-specific parameters used in flux computations

Parameter [units]	**Value(s)**	**Reference**
Arc length [km]	[2000, 3500]	Lee et al., 2013
Stratigraphic thickness [km]	3.5 (Pz), 3.5 (Tr, Jr)	Saleeby and Busby, 1993; Stevens and Greene, 1999
Arc width [km]	[300, 400]	Lee et al., 2013

Arc thickness [km]	7	--
Skarn thickness [km]	3	--
Carbonate proportion	0.23 (Pz), [.14, .34] (Tr, Jr)	Saleeby and Busby, 1993; Stevens and Greene, 1999
Siliciclastic proportion	0.77 (Pz), calculated (Tr, Jr)	Saleeby and Busby, 1993; Stevens and Greene, 1999
Mixed proportion	0 (Pz), [.15, .43] (Tr, Jr)	Saleeby and Busby, 1993; Stevens and Greene, 1999
Granitoid area addition rate [km^2/Myr]	[1000, 3000]	Cao et al., 2017
Time interval [Myr]	40	--

Table DR3. Specific parameters for Phanerozoic flux computations

Parameter [units]	**Value(s)**	**Reference**
Stratigraphic thickness [km]	Differs for each rock unit	Peters et al., 2018
Burial rate [km/Myr]	[.01, 1]	Schumer and Jerolmack, 2009
Arc thickness [km]	10	--
Time interval (Myr)	10	--

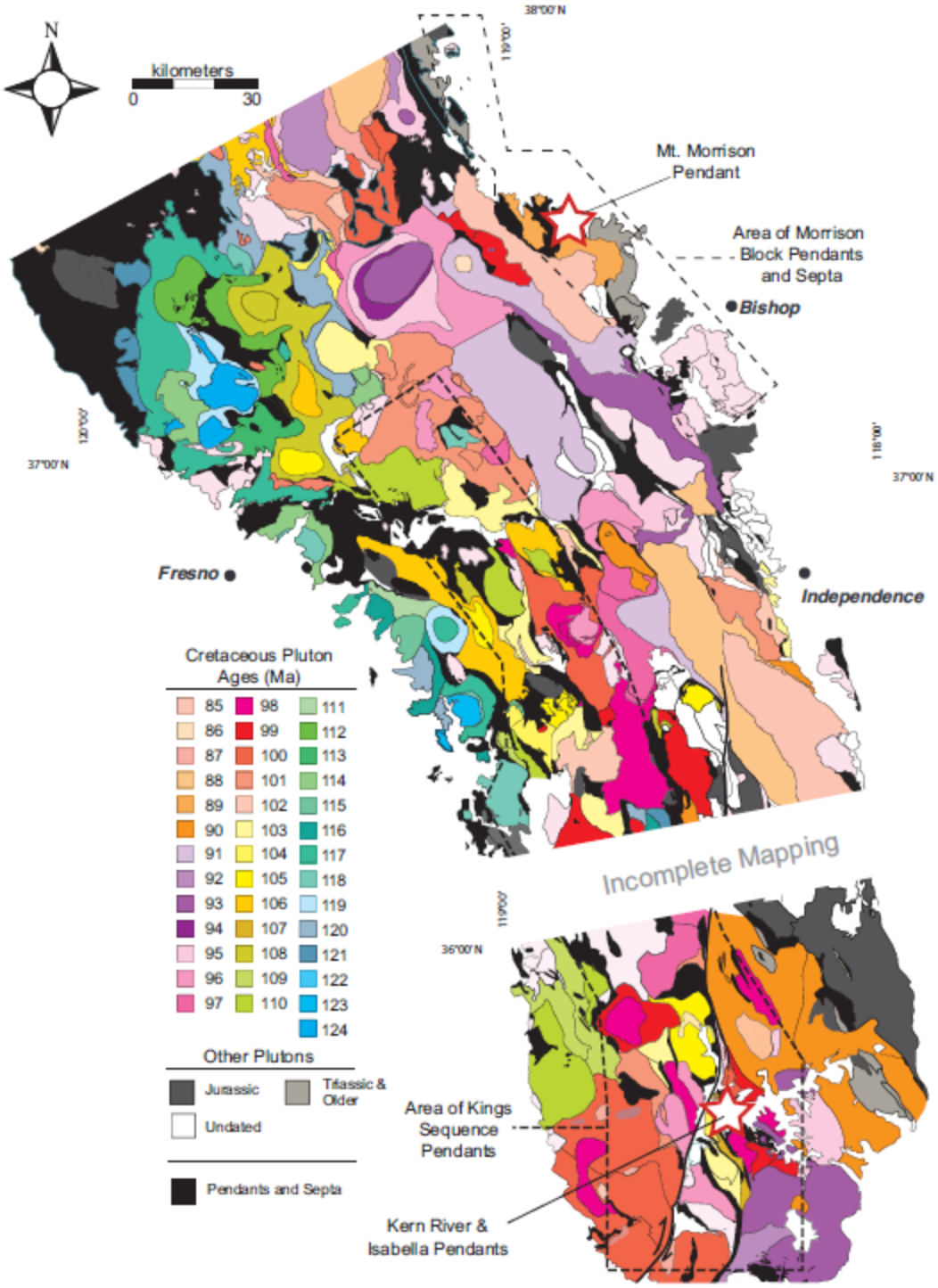

Figure DR1. Corridor of the SNB that was used for the magma and metamorphic pendant volume computations. Each color represents the mean crystallization age of the pluton. Black, gray, and white spaces are either metamorphic pendants, undated plutons, or younger cover rocks. Black dashed lines demarcate where the Kings Sequence and Morrison Block pendants crop out and the stars are the approximate locations from where the stratigraphic columns in Fig. DR2 are derived.

Figure DR2. Example Stratigraphic Columns

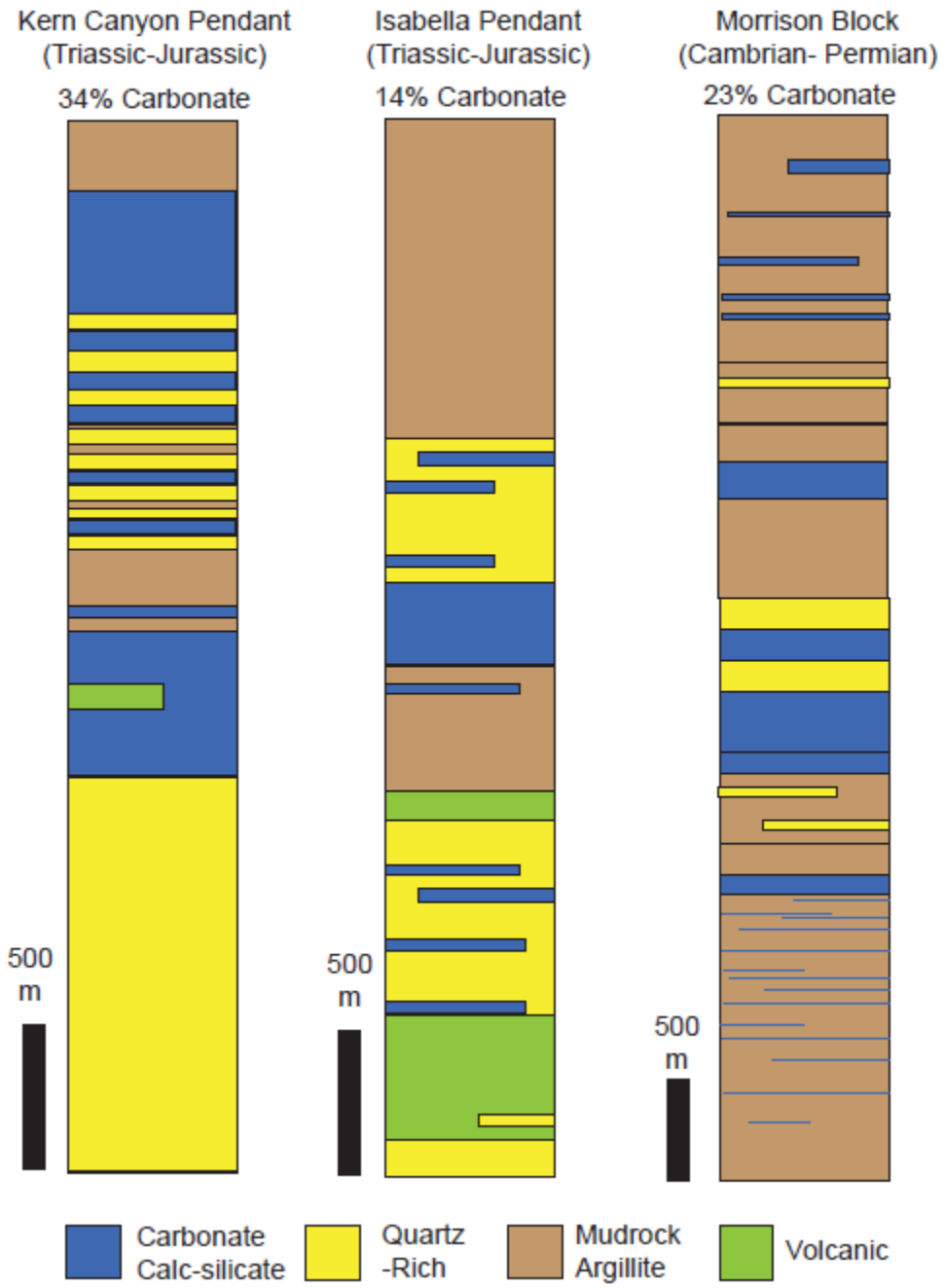

Figure DR2. Composite stratigraphic sections of typical metavolcanics and metasedimentary sections from roof pendants in the Sierra Nevada. The Kern Canyon and Isabella pendants are part of the Kings Sequence pendants.

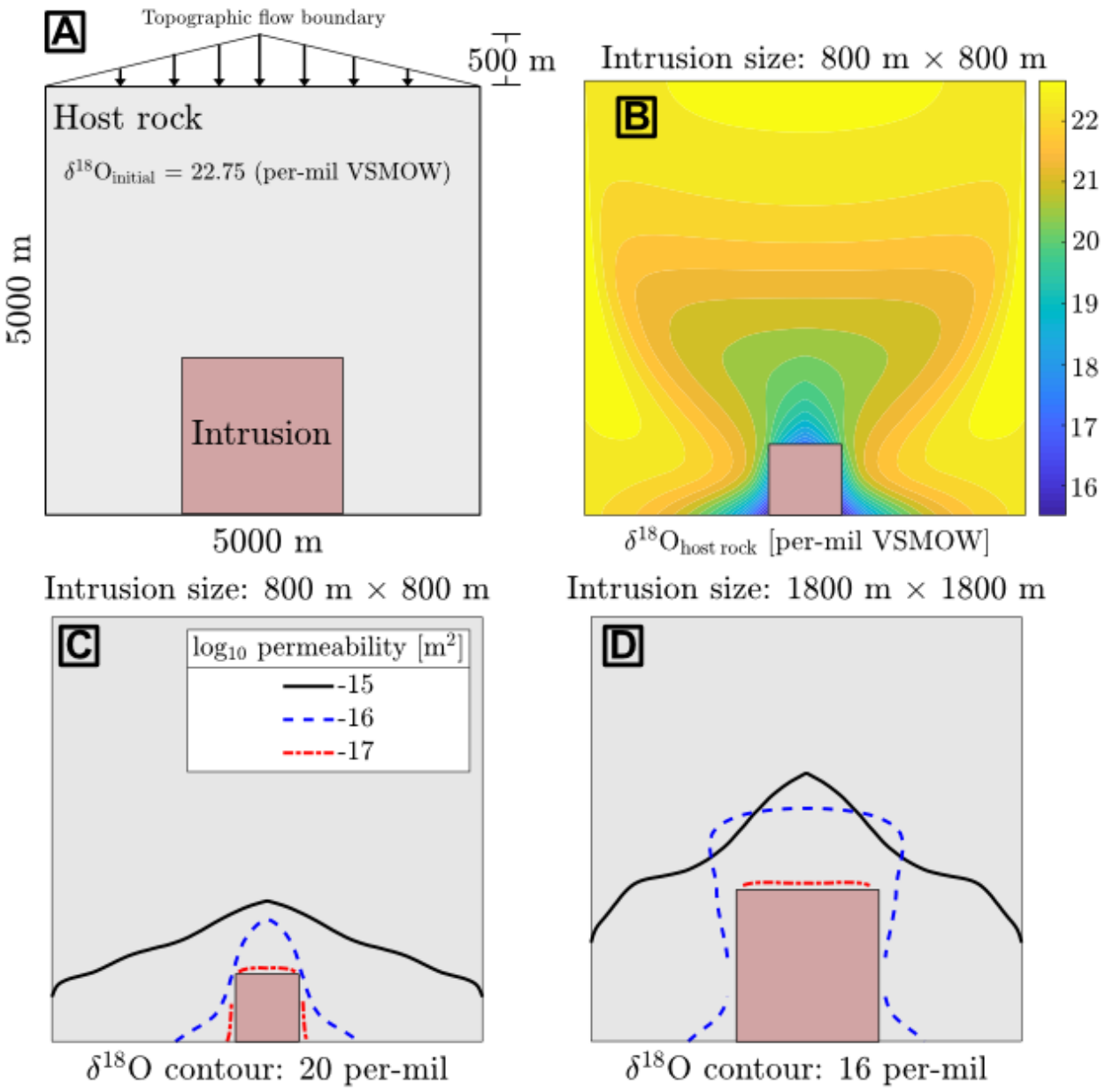

Figure DR3. Analogue model results. A) Cartoon representation of the two-dimensional domain in which the aureole volume is determined. A square intrusion is situated at the bottom center of a 5000 m x 5000 m domain comprised entirely of carbonate rock. The initial $\delta^{18}O$ value of the host rock is that of unaltered marine limestone. On the uppermost boundary, a symmetrical linear boundary condition is imposed, representative of topography-driven fluid flow. The input fluids at the uppermost surface are assumed to have a $\delta^{18}O$ values of -10‰ (description of other boundary conditions for heat flow, fluid flow, and O-isotope transport are available in Ramos et al., 2018 and its supplementary section). B) Filled contour map of predicted $\delta^{18}O$ contours at the conclusion of a simulation. The host rock permeability is uniform and constant with a value of 10^{-16} m^2. C, D) Predicted $\delta^{18}O$ contours for 800 m x 800 m and 1800 m x 1800 m intrusions, respectively, with varying host rock permeability. We select one $\delta^{18}O$ value

as the defining contour line across the simulations with varying host rock permeability. The contours illustrate the distances away from the pluton where the host rock $\delta^{18}O$ value decreased from its initial value to the value specified in the figure. In general, the higher the permeability, the farther the isotopic front is from the intrusion. The $\delta^{18}O$ values of the host rock are converted to volume fraction of decarbonated host rock following the equation in section 1E.

References

Allen, P.A. and Allen, J.R., 2013. *Basin analysis: Principles and application to petroleum play assessment*. John Wiley & Sons.

Ague, J.J., and Brimhall, G.H., 1988, Magmatic arc asymmetry and distribution of anomalous plutonic belts in the batholiths of California: effects of assimilation, crustal thickness, and depth of crystallization: Geological Society of America Bulletin, v. 100, p. 912-927.

Bateman, P.C., 1992, Plutonism in the central part of the Sierra Nevada Batholith, California: U. S. Geological Survey Professional Paper, v. 1483, p. 186.

Cao, W., Lee, C.T.A. and Lackey, J.S., 2017. Episodic nature of continental arc activity since 750 Ma: A global compilation. *Earth and Planetary Science Letters*, *461*, pp.85-95.

Carter, L.B. and Dasgupta, R., 2016. Effect of melt composition on crustal carbonate assimilation: Implications for the transition from calcite consumption to skarnification and associated CO_2 degassing. *Geochemistry, Geophysics, Geosystems*, *17*(10), pp.3893-3916.

Chen, J.H., and Moore, J.G., 1982, Uranium-lead isotopic ages from the Sierra Nevada batholith, California: JGR Journal of Geophysical Research. B, v. 87, p. 4761-4784.

Clemens-Knott, D., van der Kolk, D.A., Sturmer, D.M., and Saleeby, J.B., 2013, The Goldstein Peak Formation, central California: Record of a nonmarine intra-arc basin within the Early Cretaceous Sierra Nevada arc: Geosphere, v. 9, p. 718–735.

Ducea, M., 2001, The California Arc: thick granitic batholiths, eclogitic residues, lithospheric-scale thrusting, and magmatic flare-ups: GSA Today, v. 11, p. 4-10.

Ducea, M.N., Saleeby, J.B. and Bergantz, G., 2015. The architecture, chemistry, and evolution of continental magmatic arcs. *Annual Review of Earth and Planetary Sciences*, *43*, pp.299-331.

Fiske, R.S., and Tobisch, O.T., 1978, Paleogeographic significance of volcanic rocks of the Ritter Range pendant, central Sierra Nevada, California, *in* Howell, G, and McDougall, eds., Mesozoic paleogeography of the western United States.: Pacific Coast

Paleogeography Symposium: Los Angeles, CA, United States, Pacific Section, Society of Economic Paleontologists and Mineralogists, p. 209–221.

Frazer, R.E., Coleman, D.S., and Mills, R.D., 2014, Zircon U-Pb geochronology of the Mount Givens Granodiorite: implications for the genesis of large volumes of eruptible magma: Journal of Geophysical Research: Solid Earth, v. 119, p. 2907-2924.

Jenkins, W.O., 1943, Tungsten Deposits Northeast of Visalia, California: California Journal of Mines and Geology Bulletin, v. 39, p. 169-182.

Kelemen, P.B. and Manning, C.E., 2015. Reevaluating carbon fluxes in subduction zones, what goes down, mostly comes up. *Proceedings of the National Academy of Sciences*, *112*(30), pp. E3997-E4006.

Krauskopf, K.B., 1953, Tungsten deposits of Madera, Fresno, and Tulare Counties, California: California. Division of Mines and Geology Special Report, v. 35, p. 83.

Lackey, J.S., Cecil, M.R., Windham, C.J., Frazer, R.E., Bindeman, I.N., and Gehrels, G., 2012, The Fine Gold Intrusive Suite: The Roles of Basement Terranes and Magma Source Development in the Early Cretaceous Sierra Nevada Batholith: Geosphere, v. 8, p. 292–313.

Lackey, J.S., Valley, J.W., Chen, J.H., and Stockli, D.F., 2008, Evolving magma systems, crustal recycling, and alteration in the central Sierra Nevada batholith: the oxygen isotope record: Journal of Petrology, v. 49, p. 1397–1426.

Lee, C.T.A., Shen, B., Slotnick, B.S., Liao, K., Dickens, G.R., Yokoyama, Y., Lenardic, A., Dasgupta, R., Jellinek, M., Lackey, J.S. and Schneider, T., 2013. Continental arc–island arc fluctuations, growth of crustal carbonates, and long-term climate change. *Geosphere*, *9*(1), pp.21-36.

Lee, C.T.A., Caves, J., Jiang, H., Cao, W., Lenardic, A., McKenzie, N.R., Shorttle, O., Yin, Q.Z. and Dyer, B., 2018. Deep mantle roots and continental emergence: Implications for whole-Earth elemental cycling, long-term climate, and the Cambrian explosion. *International Geology Review*, *60*(4), pp.431-448.

Lemmon, D.M., 1940, Tungsten Deposits in the Tungsten Hills, Inyo County, California: U.S. Geological Survey Bulletin, v. 922-Q, p. 497–514.

Lemmon, D.M., 1941, Tungsten Deposits in the Sierra Nevada Near Bishop California: U.S. Geological Survey Bulletin, v. 931-E, p. 79–104.

Mackenzie, F.T. and Garrels, R.M., 1971. *Evolution of sedimentary rocks*. New York: Norton.

Moore, J.G., and Sisson, T.W., 1987, Preliminary geologic map of Sequoia and Kings Canyon national parks, California: U. S. Geological Survey Open-File Report, v. 87-0651, p. 1 Sheet, 1:250,000.

Nadin, E.S., and Saleeby, J.B., 2008, Disruption of regional primary structure of the Sierra Nevada batholith by the Kern Canyon fault system, California: Geological Society of America Special Paper, v. 438, p. 429–454.

Peters, S.E., Husson, J.M. and Czaplewski, J., 2018. Macrostrat: a platform for geological data integration and deep-time Earth crust research. *Geochemistry, Geophysics, Geosystems*, *19*(4), pp.1393-1409.

Ramos, E.J., Hesse, M.A., Barnes, J.D., Jordan, J.S. and Lackey, J.S., 2018. Reevaluating fluid sources during skarn formation: an assessment of the Empire Mountain skarn, Sierra Nevada, USA. *Geochemistry, Geophysics, Geosystems*, *19*(10), pp.3657-3672

Ronov, A.B., 1982. The Earth's sedimentary shell (quantitative patterns of its structure, compositions, and evolution) The 20th VI Vernadskiy Lecture, March 12, 1978. *International Geology Review*, *24*(11), pp.1313-1363.

Ross, D.C., 1987, Generalized geologic map of the basement rocks of the southern Sierra Nevada, California: U. S. Geological Survey Open-File Report, v. 87-0276, p. p 30.

Ross, D.C., 1989, The metamorphic and plutonic rocks of the southernmost Sierra Nevada, California, and their tectonic framework: U. S. Geological Survey Professional Paper, v. 1381, p. p 159.

Saleeby, J.B. and Busby, C., 1993. Paleogeographic and tectonic setting of axial and western metamorphic framework rocks of the southern Sierra Nevada, California. *In Dunn, G., and McDougall, K., eds., 1993, Mesozoic Paleogeography of the Western United States-II Pacific Section SEPM, Book 71*, p. 197-226.

Saleeby, J., Ducea, M.N., Busby, C., Nadin, E., and Wetmore, P.H., 2008, Chronology of pluton emplacement and regional deformation in the southern Sierra Nevada batholith, California: Geological Society of America Special Paper, v. 438, p. 297-327.

Saleeby, J., Goodin, S., Sharp, W.D., and Busby, C., 1978, Early Mesozoic paleotectonic-paleogeographic reconstruction of the southern Sierra Nevada region, *in* Howell, G., and McDougall, G., eds., Mesozoic paleogeography of the western United States.: Los Angeles, CA, United States, SEPM, Pacific Section, p. 311-336.

Schumer, R. and Jerolmack, D.J., 2009. Real and apparent changes in sediment deposition rates through time. *Journal of Geophysical Research: Earth Surface*, *114*(F3).

Sisson, T.W., and Moore, J.G., 2013, Geologic map of southwestern Sequoia National Park, Tulare County, California: U. S. Geological Survey Open-File Report 2013–1096, scale 1:24,000.

Stern, T.W., Bateman, P.C., Morgan, B.A., Newell, M.F., and Peck, D.L., 1981, Isotopic U-Pb ages of zircon from the granitoids of the central Sierra Nevada, California: U. S. Geological Survey Professional Paper v. 1185, p. 17.

Stevens, C.H. and Greene, D.C., 1999. Stratigraphy, depositional history, and tectonic evolution of Paleozoic continental-margin rocks in roof pendants of the eastern Sierra Nevada, California. *Geological Society of America Bulletin*, *111*(6), pp.919-933.

Tobisch, O.T., Fiske, R.S., Saleeby, J.B., Holt, E., and Sorensen, S.S., 2000, Steep tilting of metavolcanic rocks by multiple mechanisms, central Sierra Nevada, California: Geological Society of America Bulletin, v. 112, p. 1043-1058.